

Characterization of UWB Channel Impulse Responses within the Passenger Cabin of a Boeing 737-200 Aircraft

Simon Chiu, James Chuang and David G. Michelson, *Senior Member, IEEE*

Abstract—With its confined volume, cylindrical structure and high density of seating, the passenger cabin of a typical midsize airliner is significantly different from the residential, office, outdoor and industrial environments previously considered by IEEE 802.15.4a. We have characterized the shape of the ultrawideband (UWB) channel impulse response (CIR) and the fading statistics experienced by individual multipath components (MPCs) within that environment based upon 3300 complex frequency responses that we measured over the range 3.1–10.6 GHz at various locations aboard a Boeing 737-200 aircraft. We found that: (1) the shape of the CIR generally follows IEEE 802.15.4a’s dense single-cluster model, but with negligible rise time if the link is line-of-sight, (2) both the mean and variance of the exponential decay constant tend to increase with transmitter-receiver separation and also as the receiving antenna drops from the headrest to the footrest of the passenger seats, and (3) small-scale fading of individual MPCs at each measurement location within the aircraft tends to follow a Nakagami distribution with a lognormally-distributed m -parameter that has a mean value of 0.2 dB and a standard deviation of 1.1 dB. We have modified IEEE 802.15.4a’s CIR simulator to generate responses similar to those seen in the cabin.

Index Terms— aircraft, channel impulse response, channel model, fading channels, multipath channels, ultrawideband propagation.

I. INTRODUCTION

THE channel modeling committees of the IEEE 802.15.3a and 802.15.4a task groups devoted considerable effort to developing ultrawideband (UWB) wireless channel models applicable to systems that operate between 3.1 and 10.6 GHz under both line-of-sight (LOS) and non-line-of-sight (NLOS) conditions in residential, office, outdoor, industrial and body-centric environments at ranges up to 15 m. The standard channel models and channel impulse response (CIR) simulator that they developed allow fair comparison between alternative

UWB systems over a range of representative channel conditions and deployment scenarios [1]-[3].

So that developers can effectively predict and compare the performance of UWB wireless communication systems in an environment of interest, both the shape and structure of the CIR, and the small-scale fading statistics experienced by individual multipath components (MPCs) within the CIR, must be accurately modeled. The results affect many important design issues, including selection of the number and placement of the fingers in rake receivers used to implement temporal diversity in spread spectrum systems and the selection of the guard-time and the design of cyclic prefixes used to mitigate multipath fading in OFDM systems. Because unclustered CIR models tend to overestimate link capacity if the MPCs are indeed clustered, it is useful to determine the extent to which clustering occurs [4]. The shape of the CIR also affects the performance of UWB ranging and positioning algorithms because it determines how well the algorithm will be able to detect the first arriving MPC. In practice, the CIR is often expressed in the form of a power delay profile (PDP) that excludes the phase information associated with each MPC.

UWB wireless systems hold great promise for: (1) enabling high data rate in-flight entertainment (IFE) and network access within the passenger cabin of an aircraft and (2) facilitating operations and maintenance through deployment of low power UWB-based sensor networks [5]. Early concerns that UWB-based systems would interfere with aircraft systems have largely been allayed by recent NASA studies [6],[7]. However, with its confined volume, cylindrical structure and high density of seating, an aircraft passenger cabin is fundamentally different from previously modeled UWB propagation environments. Although several research groups have made considerable progress in characterizing aircraft passenger cabins in support of deployment of conventional wireless technologies [8]-[14], and a few groups, including us, have reported results regarding large-scale aspects of UWB propagation in aircraft passenger cabins [15],[16], little has been reported concerning the detailed structure of UWB CIRs and the fading and correlation properties of their MPCs in such environments.

Manuscript received January 6, 2009; revised April 9, 2009; revised July 3, 2009; accepted July 22, 2009.

S. Chiu, J. Chuang and D. G. Michelson are with the Radio Science Laboratory, Department of Electrical and Computer Engineering, University of British Columbia, Vancouver, BC, Canada V6T 1Z4. Corresponding author: D. G. Michelson, tel: 604 822-3544, fax: 604 822-5949, email: davem@ece.ubc.ca.

This work was supported in part by grants from Nokia Products, Bell Canada (through its Bell University Labs program), and Western Economic Diversification Canada.

Here, we characterize the shape and structure of the UWB CIR, and the fading statistics and correlation properties of individual MPCs within the passenger cabin of a typical mid-sized airliner with the intent of developing a UWB CIR simulation model useful in analysis and design. Our results are based upon over 3300 complex channel frequency responses (CFRs) that we measured over the range 3.1 – 10.6 GHz aboard a Boeing 737-200 aircraft with an omnidirectional transmitting antenna mounted near the cabin ceiling and an omnidirectional receiving antenna mounted at selected locations throughout the cabin. We refer to this as a *point-to-multipoint* (p-to-mp) configuration. So that we could assess the spatial statistics of the UWB CIR, *i.e.*, the spatial average and the spatial correlation, we collected the CIRs across a 300-mm-by-300-mm spatial sampling grid with 50-mm spacing.

The remainder of this paper is organized as follows. In Section II, we describe the configuration and calibration of our VNA-based channel sounder, our procedure for collecting channel frequency response (CFR) data in the aircraft and our measurement database. In Section III, we present our proposed model for the shape and structure of the PDPs that we observed within the aircraft passenger cabin. In Section IV, we report upon the fading statistics experienced by MPCs and the fading correlation between MPCs that are either: (1) in adjacent delay bins with the antenna at the same point on the sampling grid or (2) in the same delay bin but with the antenna at an adjacent point on the sampling grid. In Section V, we describe how we modified the standard channel impulse response simulation code developed by IEEE 802.15.4a to generate CIRs representative of those observed in the aircraft passenger cabin environment and verified that its output is consistent with our measurement results. Finally, in Section VI, we summarize our key findings and contributions.

II. MEASUREMENT APPROACH

A. UWB Channel Sounder Configuration and Calibration

Our UWB channel sounder consists of an Agilent E8362B vector network analyzer (VNA), 4-m FLL-400 SuperFlex and 15-m LMR-400 UltraFlex coaxial cables, a pair of Electrometrics 6865 UWB omnidirectional biconical antennas, a 0.5-m-by-0.5-m two-dimensional antenna positioner based upon Velmex BiSlide positioning slides, the tripods and fixtures that we used to mount the antennas at various locations throughout the cabin, and a laptop-based instrument controller equipped with a GPIB interface. During data collection, a MATLAB script running on the laptop controlled both the VNA and the two-dimensional positioner, and logged the received data.

We configured the VNA to sweep from 3.1 to 10.6 GHz in 6401 steps with an IF bandwidth of 3 kHz. The resulting displayed average noise level (DANL) is -107.2 dBm. In order to meet RF emission limits imposed upon us by the Research Ethics Boards at the University of British Columbia and the British Columbia Institute of Technology for the human

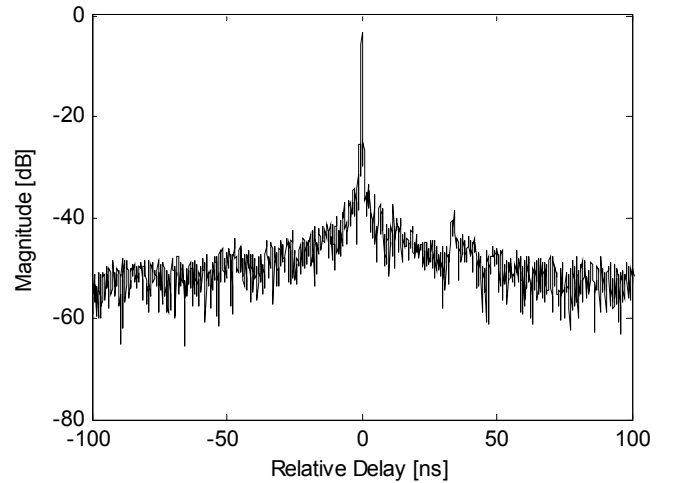


Fig. 1. Temporal resolution and dynamic range of the channel sounder after through-line calibration and application of a Kaiser window with $\beta = 7$, and after the RF cables have undergone moderate flexion and torsion.

TABLE I
LINK BUDGET FOR THE UWB CHANNEL SOUNDER

| Links | Values | | |
|-------------------------------|------------|------------|------------|
| | 3.1 GHz | 6.85 GHz | 10.6 GHz |
| Transmitted Power | 5 dBm | 5 dBm | 5 dBm |
| Transmit Cable Loss | 1.2 dB | 1.9 dB | 2.4 dB |
| Average Transmit Antenna Gain | 0 dBi | 0 dBi | 0 dBi |
| Path Loss at 15 m* | 72.4 dB | 79.9 dB | 84.1 dB |
| Average Receive Antenna Gain | 0 dBi | 0 dBi | 0 dBi |
| Receive Cable Loss | 4.5 dB | 7.0 dB | 9.1 dB |
| Received Power | -73.1 dBm | -83.8 dBm | -90.6 dBm |
| Receiver Sensitivity | -107.2 dBm | -107.2 dBm | -107.2 dBm |
| System Margin | 34.1 dB | 23.4 dB | 16.6 dB |

*Calculated using a path loss exponent of 2.2

presence study to be conducted as a follow-on to the present work, we set the transmit power to 5 dBm. The frequency sampling interval of 1.1716 MHz corresponds to a maximum unambiguous excess delay of 853 ns or a maximum observable distance of 256 m. The frequency span of 7.5 GHz corresponds to a maximum temporal resolution of 133 ps or a maximum spatial resolution of 40 mm. In Table I, we give the principal elements of the system link budget at 3.1, 6.85 and 10.6 GHz, *i.e.*, the bottom, mid-point and top of the UWB frequency band for a transmitter-receiver separation distance of 15 m. The average antenna gain refers to the average over all angles and directions. The path loss exponent of 2.2 used in the Table is the worst case that we observed both here and in our previous work [15]. We used through-line calibration to remove the frequency distortion introduced by the VNA and the coaxial cables that connect the VNA to the transmitting and receiving antennas. We applied a Kaiser window with $\beta = 7$ to the CFRs in order to suppress dispersion of energy into adjacent delay bins. After applying moderate flexion and torsion to the RF cables, we applied a Fourier transform to the resulting complex frequency response in order to reveal the resolution and dynamic range of the instrument under typical conditions. The result is shown in Figure 1.

The transmitting and receiving antennas are vertically

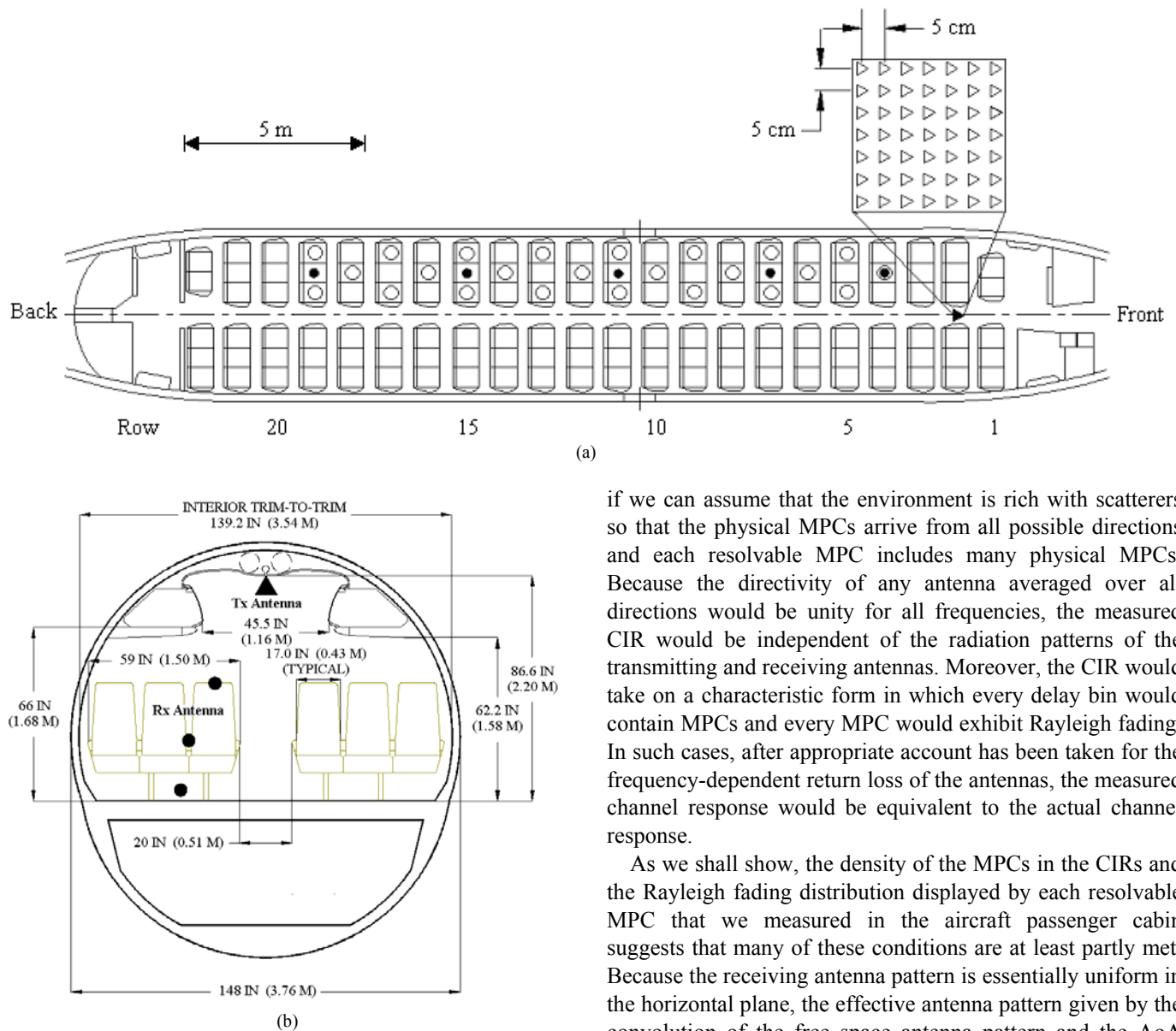


Fig. 2. Locations of the transmitting antenna (►) and receiving antennas (o = headrest and armrest, ● = footrest) within a Boeing 737-200 aircraft in (a) plan and (b) cross-section view.

polarized, omnidirectional and identical. The measured channel response includes elements of both the actual response of the *propagation channel* and the response of the transmitting and receiving antennas. This result is often referred to as the response of the *radio channel*. In order to perfectly de-embed the propagation channel response from the radio channel response, one would need to measure the frequency-dependent double-directional channel response that accounts for the angle-of-departure (AoD) and angle-of-arrival (AoA) of each ray and the frequency-dependent three-dimensional radiation pattern of each antenna [2]. Implementing the required measurement setup within the confines of the aircraft passenger cabin would be problematic, however.

The antenna calibration problem is simplified considerably

if we can assume that the environment is rich with scatterers so that the physical MPCs arrive from all possible directions and each resolvable MPC includes many physical MPCs. Because the directivity of any antenna averaged over all directions would be unity for all frequencies, the measured CIR would be independent of the radiation patterns of the transmitting and receiving antennas. Moreover, the CIR would take on a characteristic form in which every delay bin would contain MPCs and every MPC would exhibit Rayleigh fading. In such cases, after appropriate account has been taken for the frequency-dependent return loss of the antennas, the measured channel response would be equivalent to the actual channel response.

As we shall show, the density of the MPCs in the CIRs and the Rayleigh fading distribution displayed by each resolvable MPC that we measured in the aircraft passenger cabin suggests that many of these conditions are at least partly met. Because the receiving antenna pattern is essentially uniform in the horizontal plane, the effective antenna pattern given by the convolution of the free space antenna pattern and the AoA distribution in that plane is also uniform regardless of the actual AoA distribution. Thus, this condition is automatically met. However, the receiving antenna pattern in the vertical plane is decidedly non-uniform so the effective antenna pattern will be uniform only if the actual AoA distribution is uniform. Previous work in conventional indoor environments has shown that the AoA distribution in the vertical plane broadens considerably as the size of the enclosed space becomes smaller [17]. While this suggests that the AoA distribution in the vertical plane within the aircraft is likely to be broad, it is not likely to be uniform. Other previous work using the same biconical antennas found remarkable differences in the spatial correlation between 2 and 12 GHz, which were also related to differences in the antenna patterns, particularly in the vertical plane [18]. In such work, when the frequency was increased, the spatial correlation was increased as well (for the same wavelength), which indicated higher directivity on radio channels, and lower delay spread. Thus, although we believe that our measured CIR provides a

reasonable indication of the actual CIR, our results strictly apply to the radio channel and slightly different results may be obtained if other transmitting and receiving antennas with different radiation patterns in the vertical plane are used.

B. Data Collection

We collected our CFR measurements within the passenger cabin of a Boeing 737-200 aircraft. The cabin, which can seat over 100 passengers, is 3.54 m in width, 2.2 m in height and 21 m in length of which 18 m actually includes passenger seating. Plan and cross-sectional views of the passenger cabin are shown in Figure 2(a) and (b), respectively. Other modern mid-sized airliners, such as the CRJ series from Bombardier, the A320 family from Airbus Industries and the ARJ21 family from ACAC, have similar cross-sections. Only the lengths of the passenger cabins, which range from 12 to 43 m, are appreciably different.

Here, we have considered a p-to-mp wireless system configuration in which the transmitting antenna is mounted along the centerline of the cabin ceiling in the manner of an access point and the receiving antenna is placed at the headrest, armrest and footrest level of the passenger seats throughout the aircraft, as suggested by Figure 2(a) and (b). The different receiving antenna mounting positions not only represent typical use cases such as using a cell phone (at headrest level), a laptop (at armrest level) or devices that might be contained in passengers' carry-on baggage (at footrest level) but also represent both LOS (at the headrest and aisle armrest) and NLOS (at the outboard armrest and footrest) channels.

In Section IV, we present MPC fading statistics within a local area that we estimated using methods similar to those described in [3]. Although standard practice would be to move the receiving antenna across the spatial sampling grid, this is difficult to do when the antenna is mounted close to the passenger seats. Because moving the transmitting antenna instead was shown to yield good results in [4], we did so here, too. With the receiving antenna mounted at headrest, armrest and footrest levels, we collected 49 spatial samples by mounting the transmitting antenna at ceiling level at row 2 and moving it across a 7-by-7 grid with a spacing of 50 mm, as shown in Figure 2(a). By setting the spacing equal to half of the wavelength of the lowest frequency, we sought to ensure that the spatial samples are independent. This, however, does not allow unambiguous resolution of the direction of a given ray, which requires the spacing be equal to half of a wavelength at the highest frequency [2]. Previous work suggests that: (1) approximately nine samples are sufficient to average out the small-scale fading and permit the true shape of the PDP to be recovered [19], and (2) approximately 50 samples are sufficient to determine the underlying fading distribution [2]. Here, we have elected to use 49 spatial samples per measurement location because it permits use of a symmetrical 7-by-7 sampling grid.

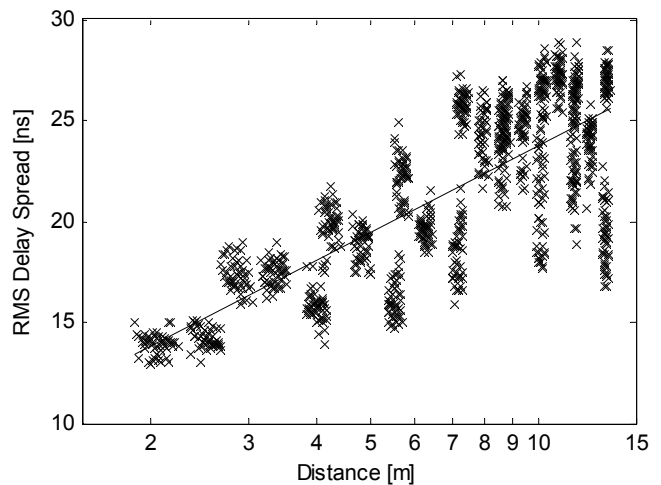


Fig. 3. RMS delay spread as a function of distance when the receiving antenna is mounted on the headrest.

C. Consistency Checks

Before we collected production data, we conducted a series of development runs in order to: (1) verify that the channel is static and show that we could exploit the bilateral and translational symmetry inherent in the cabin layout to dramatically reduce the number of measurements needed to characterize propagation within the aircraft, and (2) verify that the shape and structure of the CIRs are consistent within a local area and that any differences between the CIRs that we observed over that local area are mostly due to multipath fading of individual MPCs. We did so by comparing: (1) the shapes of the average power delay profiles (APDPs) based upon CIRs measured at nine points on a 100-mm-by-100-mm grid with the receiving antenna mounted at rows 4, 7, 11, 15 and 19, and (2) the mean excess delay, τ_{mean} , and RMS delay spread, τ_{rms} , based upon CIRs measured at 49 points on a 300-mm-by-300-mm grid with the receiving antenna mounted at rows 4, 11 and 19. The mean excess delay and RMS delay spread were calculated using a threshold of 25 dB below the peak scattered component. Although it is difficult to set an absolute criterion for consistency, support for the conjecture is given by: (1) visual inspection of the APDPs and the plot of RMS delay spread vs. distance in Figure 3 and (2) observation that the standard deviations of the mean excess delay and RMS delay spread over all measurement locations are, on average, less than 1.5 and 1 ns, respectively. In Section III-A, we describe the details of the processing steps that we followed when estimating APDPs from measured CIRs.

D. Measurement Database

Our measurement database includes both development and production data. During our development runs, we collected two sets of data. In the first set, we considered three transmitter locations and over 50 receiver locations. For selected paths, we collected multiple sweeps in succession and verified that: (1) the channel is static and (2) our channel sounder yielded consistent results. In the second set, we used a single transmitter location and we measured the channel

response at five locations across either 9-point or 49-point spatial sampling grids with the receiving antenna placed at headrest, armrest and footrest levels. The two sets combine to yield over 700 CFRs.

During our production runs, we placed the receiving antenna at headrest, armrest and footrest levels throughout the port side of the cabin. When we mounted the receiving antenna at the headrest and armrest, we collected the CFRs at 24 different locations and when we mounted the antenna at the footrest level, we collected CFRs at five locations. These measurement locations are shown in Figure 2. In both cases, we used a 49-point spatial sampling grid, yielding 2597 CFRs. In total, our development and production runs yielded over 3300 CFRs.

III. SHAPE AND STRUCTURE OF THE POWER DELAY PROFILE

A. Initial Processing of the Channel Impulse Response

Whether measured in the time or frequency domain, a measured channel response has a finite bandwidth that is determined by either the instrument or the measurement process. The result is equivalent to convolving the true CIR with a sinc function whose duration is inversely proportional to the bandwidth of the measurement. Before processing a measured CIR, one must first remove the effects of the finite bandwidth either by windowing or deconvolution. Here, we applied a Kaiser window with $\beta = 7$ to the CFRs in order to suppress dispersion of energy into adjacent delay bins. We converted the CFRs into complex baseband CIRs by applying an inverse Fourier transform (IFT).

We normalized the CIRs so that they contained unit energy. Because we know the precise separation between the transmitter and receiver, it was a simple matter to determine the propagation delay, τ_0 , and then set the start time of the first arriving MPC to zero. (When the precise separation is not known, previous workers have defined the start of a LOS CIR as the first MPC that arrives within 10 dB of, and 10 ns before, the peak MPC. They further defined the start of a NLOS CIR as the first MPC that arrives within 10 dB of, and 50 ns before, the peak MPC. Such an approach is not required here.) After we removed the initial delays, we aligned the first arriving MPCs in each PDP and averaged the MPCs directly in the time domain to yield the small-scale APDP [20],[21]. Unless otherwise indicated, we removed all MPCs with amplitudes that are more than 25 dB below the peak MPC before we extracted any model parameters. These criteria are based upon those cited in [4] and employed by the IEEE 802.15.4a channel modeling committee.

As others have noted, the fine delay resolution of a UWB PDP may cause a physical MPC that arrives at a certain delay when observed at a certain grid point to fall in a different delay bin when observed at another grid point [2],[21]. Although the process of averaging will smear the PDP, the result will affect dense single cluster PDPs (in which a resolvable MPC consists of several physical MPCs) differently than sparse multi-cluster PDPs (in which a

resolvable MPC may correspond to a single physical MPC and many delay bins are empty). Following the method described in [20], we reduced our delay resolution by a factor of 10, *i.e.*, from 133 ps to 1.33 ns in order to reduce the smearing effect. We observed that the APDPs with reduced time resolution present the same shape and structure as the original APDPs.

B. IEEE 802.15 CIR Models

Our next task was to identify the channel impulse response model that offers the best description of time dispersion within the aircraft passenger cabin. We began by considering the two standard UWB channel models that were adopted by the IEEE 802.15.3a and 4a task groups [1],[3]. The sparse multi-cluster model is based upon the SV model given by

$$h(t) = \sum_{l=1}^L \sum_{k=1}^K a_{k,l} \exp(j\phi_{k,l}) \delta(t - T_l - \tau_{k,l}). \quad (1)$$

Here, the MPCs are modeled as Dirac delta functions, $\delta(\cdot)$, and $a_{k,l}$ and $\phi_{k,l}$ are the amplitude and phase of the k th MPC in the l th cluster, L is the total number of clusters in the CIR and K is the total number of MPCs within the l th cluster. T_l and $\tau_{k,l}$ represent the arrival time of the l th cluster and the k th MPC in the l th cluster, respectively. Because path loss is frequency dependent, the MPCs are distorted as described in [2],[3]. IEEE 802.15.4a used a modified form of the SV model that accounts for such distortion to describe the UWB CIRs in six of the eight scenarios they considered. The shape of the corresponding PDP is described by the product of two exponential functions,

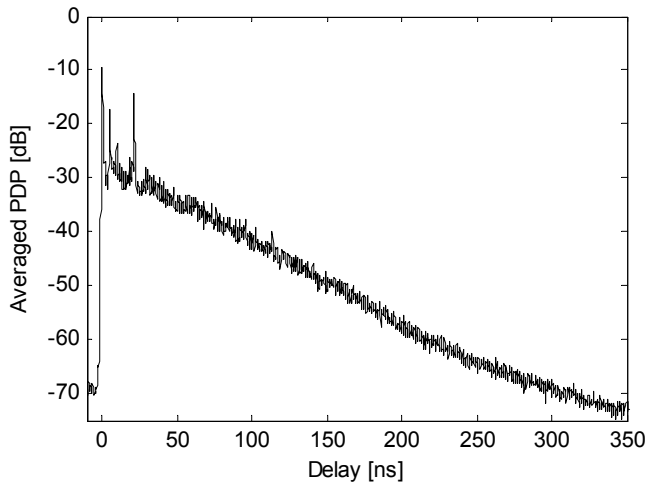
$$E\{|a_{k,l}|^2\} \propto \exp(-T_l/\Gamma) \exp(-\tau_{k,l}/\gamma_m), \quad (2)$$

where Γ and γ_m are the inter-cluster and intra-cluster decay constants, respectively.

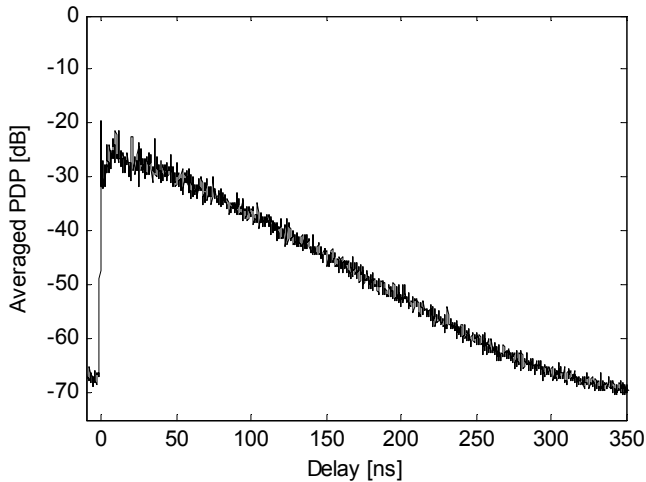
The dense single-cluster model is used to describe dense scattering environments, *e.g.*, the office and industrial environments under NLOS conditions. In these environments, one can no longer discern clustering within the CIR and the envelope of the PDP can be described as

$$E\{|a_{k,l}|^2\} \propto \left(1 - \chi \exp\left(\frac{-\tau_{k,l}}{\gamma_{rise}}\right)\right) \exp\left(\frac{-\tau_{k,l}}{\gamma_1}\right), \quad (3)$$

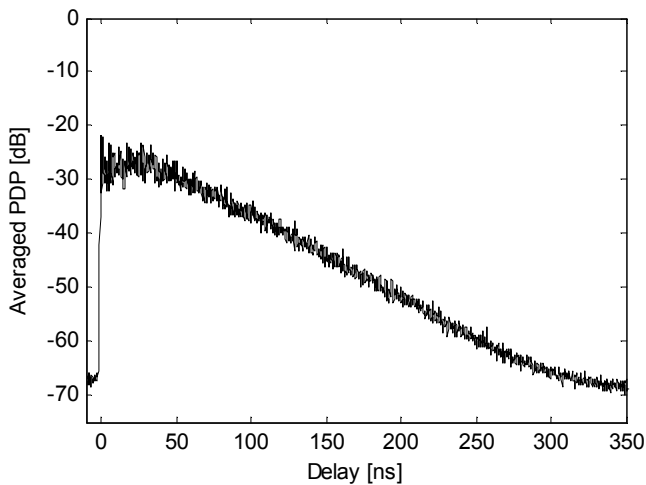
where χ denotes the attenuation of the first component, γ_{rise} determines how fast the PDP rises to its local maximum and γ_1 represents the decay at later times [3]. If the scattering environment is sufficiently dense, *e.g.*, an industrial NLOS environment, then every time resolution bin contains an MPC. Accordingly, the PDP can be modeled as a tapped delay line with a fixed arrival time, Δt , that is given by the inverse of the signal bandwidth. Where scatterers are less dense but the single cluster response still applies, *e.g.*, an office NLOS environment, then the convention is to model the arrival rate



(a)



(b)



(c)

Fig. 4. The spatially averaged PDP observed when the receiving antenna is mounted at row 19 on (a) the headrest, (b) the outboard armrest and (c) the footrest.

of the MPCs by a Poisson distribution [3].

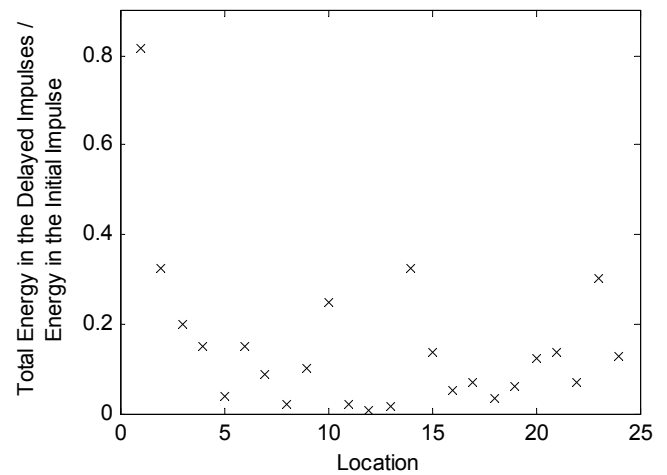


Fig. 5. Linear ratio of the total energy in the delayed impulses to the energy in the initial impulse. The initial impulse corresponds to line-of-sight propagation while the delayed impulses likely result from specular reflection in the cabin.

C. Modeling the Shape of the Power Delay Profile

In Figure 4(a), we present a typical APDP of a LOS channel based upon measurement data collected when the transmitting antenna was mounted near the cabin ceiling and the receiving antenna was mounted on the headrest of a passenger seat. When the receiving antenna is mounted on the armrest of an aisle seat, the resulting channel is also LOS and the CIR resembles that of the headrest. As in the case of industrial LOS channels, the MPCs form a continuous exponential decay with no distinct clusters. In many cases, we observed a few strong spikes or impulses early in the APDP, as described below.

In Figure 4(b) and (c), we present typical APDPs observed over NLOS channels where the receiving antenna was mounted on an outboard armrest or footrest, respectively. Similar to industrial NLOS channels, both cases display a gentle rise before reaching the local maximum described by the dense single cluster model. We also observe that the footrest case exhibits a slower rise time than the armrest case. This is likely because the initial MPCs in the footrest case encounter more and/or denser obstacles and thus are more severely attenuated than the initial MPCs in the armrest case.

Based upon our measurement results, we propose the following model for the PDP of LOS channels in aircraft passenger cabins, *i.e.*, where the receiving antenna is mounted on a headrest or aisle armrest. First, we model the shape of the scatter components of the APDP as a simple exponential decay,

$$E\{|a_k|^2\} \propto \exp\left(\frac{-\tau_k}{\gamma}\right), \quad (4)$$

where γ is the exponential decay constant. Next, we model the excess amplitude of the LOS MPC above the exponential decay curve at the propagation delay, τ_0 . In linear units, we

TABLE II
POWER DELAY PROFILE MODEL PARAMETERS - LOS CASES
(HEADREST AND AISLE ARMREST)

| Model Parameters | Headrest | | Armrest |
|------------------|-----------|-----------|-----------|
| | Aisle | Others | |
| γ_0 | 15.75 ns | | 16.02 ns |
| β_γ | 1.16 | | 1.23 |
| σ_γ | 1.10 ns | | 1.22 ns |
| Δ_0 | 23.03 dB | 23.54 dB | 15.40 dB |
| β_Δ | -0.06 | 0.59 | 0.58 |
| σ_Δ | 1.95 dB | 2.47 dB | 2.14 dB |
| d | 2 to 13 m | 2 to 13 m | 2 to 13 m |

TABLE III
POWER DELAY PROFILE MODEL PARAMETERS - NLOS CASES
(OUTBOARD ARMREST AND FOOTREST)

| Model Parameters | Armrest | Footrest |
|------------------|-----------|-----------|
| χ_0 | 0.116 | -0.143 |
| β_χ | 0.0223 | 0.0629 |
| σ_χ | 0.0397 | 0.0242 |
| γ_r | 4.86 ns | -6.34 ns |
| β_r | 0.697 | 2.61 |
| σ_r | 0.657 ns | 0.409 ns |
| γ'_0 | 12.7 ns | 13.7 ns |
| β'_γ | 1.54 | 1.50 |
| σ'_γ | 0.648 ns | 1.03 ns |
| d | 2 to 13 m | 2 to 13 m |

define the excess amplitude as

$$\Delta = P_{\text{LOS}} / \exp\left(\frac{-\tau_0}{\gamma}\right), \quad (5)$$

where P_{LOS} is the power in the LOS component and the denominator is the expected power at the beginning of the exponential decay described using (4).

On LOS channels, we often observe random impulses within the first 30 ns of the initial response. We suspect that they are due to specular reflection from the cabin bulkhead or floor and note that similar impulses have been observed in industrial environments [21]. The ratios of the energy in the initial (LOS) and delayed impulses in the APDPs that we observed when the receiving antenna is mounted on the headrest are shown in Figure 5. The delayed impulses contain only a very small fraction of the energy in the CIR and, on average, carry only 15% of the energy in the LOS component. The development of a statistical model that captures their occurrence, amplitude distribution and arrival rate would require much more data than we have available. Accordingly, we leave further efforts to model them for future study.

Although the IEEE 802.15.4a channel modeling committee did not account for the distance dependence of the CIR model parameters, we have done so here. In UWB scenarios, increases in RMS delay spread with distance are generally associated with a decrease in the SV model's cluster decay constant, Γ , or the single cluster model's exponential decay constant, γ . Using methods similar to those employed in [22] and [23], we model the variation in the exponential decay constant γ and the excess amplitude Δ with distance for LOS channels by

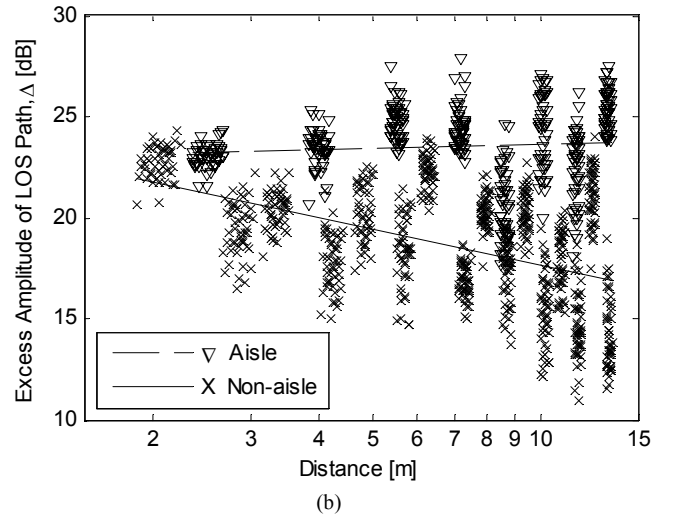
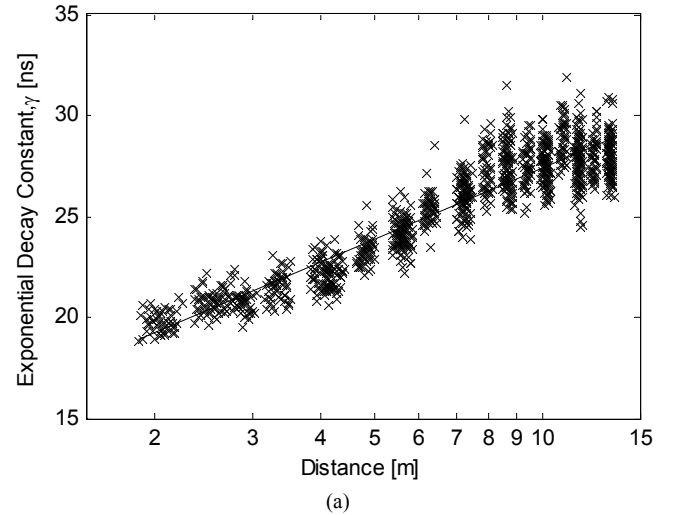


Fig. 6. Shape parameters of the power delay profile as a function of distance for headrest channels: (a) the exponential decay constant, γ , and (b) the excess amplitude of the LOS path, Δ .

$$\gamma = \gamma_0 + \beta_\gamma \cdot 10 \log_{10} d + X_\gamma \quad (6)$$

and

$$10 \log_{10} \Delta = 10 \log_{10} \Delta_0 - \beta_\Delta \cdot 10 \log_{10} d + X_\Delta, \quad (7)$$

where γ_0 and $10 \log_{10} \Delta_0$ are the intercepts, β_γ and β_Δ are the slopes, X_γ and X_Δ are zero-mean Gaussian random variables with standard deviations σ_γ and σ_Δ , respectively, and d is the distance between the transmitting and receiving antennas. The regression lines given by (6) and (7) are shown in Figure 6(a) and (b), respectively. The regression lines for the exponential decay constant for the aisle and non-aisle cases are essentially identical so we have treated the two cases as a single case in Figure 6(a). The regression lines for the excess amplitude of the LOS component for aisle and non-aisle cases are quite different so we have presented them separately in Figure 6(b). Both X_γ and X_Δ are generally well described by zero-mean normal distributions in ns and dB, respectively, and pass the

TABLE IV
SMALL-SCALE FADING PARAMETERS

| Model Parameters | Headrest | Armrest | | Footrest |
|------------------|----------|----------|----------|-----------|
| | | Aisle | Outboard | |
| μ_m | 0.311 dB | 0.247 dB | 0.342 dB | -0.194 dB |
| σ_m | 1.17 dB | 1.21 dB | 1.16 dB | 1.23 dB |
| m_{00} | 20.83 dB | 21.98 dB | — | — |
| β_{m0} | 0.702 | 0.707 | — | — |
| σ_{m0} | 2.47 dB | 2.74 dB | — | — |

Anderson-Darling goodness-of-fit test at the 5% significance level in most cases and at the 1% level in all cases except one. The bell-shaped distribution presented by X_Δ in the aisle-headrest case does not pass; it is skewed towards higher values and exhibits positive kurtosis. Our measurement data is insufficient to explain this single instance. Further study of this scenario, perhaps using ray-tracing methods, may be warranted. A summary of the LOS channel model parameters that we extracted is given in Table II.

For NLOS channels, *i.e.*, the receiving antenna mounted upon an outboard armrest or a footrest, we modeled the envelope of the PDP using (3). We describe the distance dependence of the parameters by

$$\chi = \chi_0 - \beta_\chi \cdot 10 \log_{10} d + X_\chi, \quad (8)$$

$$\gamma_{rise} = \gamma_r + \beta_r \cdot 10 \log_{10} d + X_r, \quad (9)$$

and

$$\gamma_1 = \gamma'_0 + \beta'_\gamma \cdot 10 \log_{10} d + X'_\gamma. \quad (10)$$

In (8), (9) and (10), χ_0 , γ_r and γ'_0 are the intercepts and β_χ , β_r and β'_γ are the slopes. X_χ , X_r and X'_γ are zero-mean Gaussian random variables with standard deviations, σ_χ , σ_r and σ'_γ , respectively, and d is the distance between the transmitting and receiving antennas. A summary of the NLOS channel model parameters that we extracted is given in Table III.

IV. SMALL-SCALE FADING AND INTERDEPENDENCE OF MPCs

A. Small-Scale Fading

We determined the distribution that best describes the small-scale fading of individual MPCs by processing the CIRs that we sampled at 49 points within a 300-mm x 300-mm grid, extracting the amplitudes of the taps over all delays, computing the corresponding CDFs, and comparing them to standard distributions. In the past, others have found that the small scale fading distributions observed in residential environments are well approximated by a lognormal distribution [23] while others have found that a Nakagami distribution fits well [3]. However, our results show that the small-scale fading distribution of individual MPCs in the aircraft environment is well-approximated by a Rayleigh distribution. This is a reasonable outcome given that the aircraft passenger cabin is a dense scattering environment and it is likely that each delay bin or MPC consists of several rays.

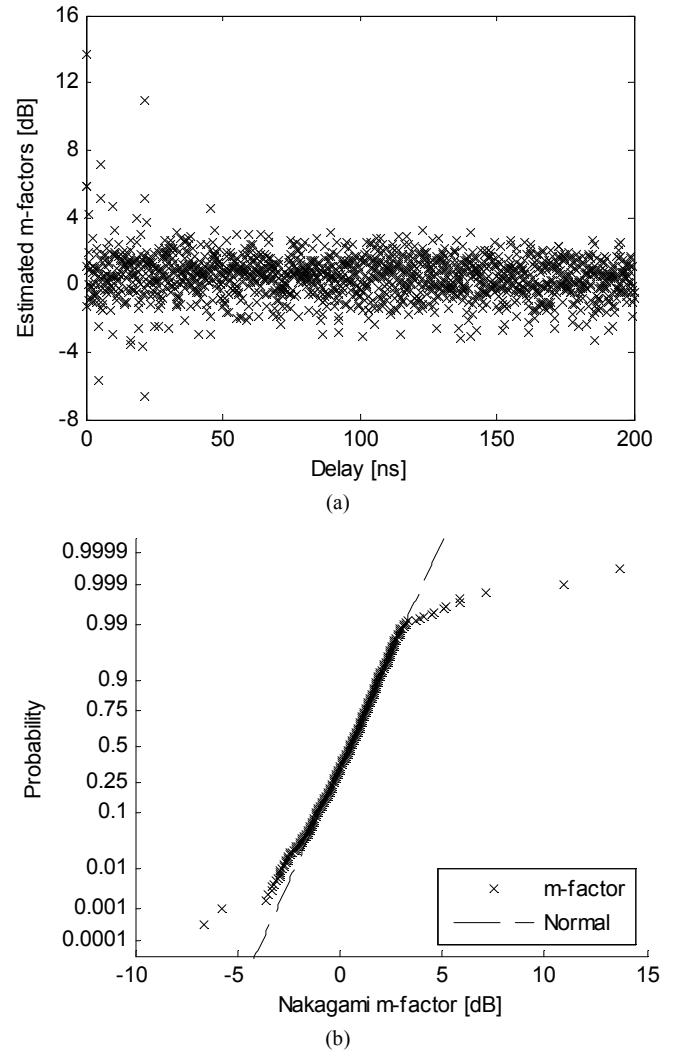


Fig. 7. Estimates of the m -factors (in dB) that describe the MPC fading distribution when the receiving antenna was mounted on the headrest of row 19: (a) as a function of delay and (b) expressed as a CDF and compared to the best fit normal distribution.

Moreover, others have reported that small-scale fading follows Rayleigh statistics in other dense scattering environments such as industrial plants [21].

We refined our understanding of the distribution of small-scale fading by fitting it to the more general Nakagami distribution that has been used to model small-scale fading in other UWB environments. The Nakagami distribution is given by

$$f_x(x) = \frac{2}{\Gamma(m)} \left(\frac{m}{\Omega}\right)^m x^{2m-1} \exp\left(-\frac{m}{\Omega} x^2\right), \quad (11)$$

where $m \geq \frac{1}{2}$ is the Nakagami m -factor (or the shape parameter of the distribution), $\Gamma(m)$ is the Gamma function, and Ω is the mean-squared value of the amplitude (or the spread parameter of the distribution). For each delay bin, we estimated the m -factor of the Nakagami distribution by applying the inverse normalized variance estimator [24] to the

49 spatial samples. The estimate of the m -factor is given by

$$\hat{m} = \frac{\mu_2^2}{\mu_4 - \mu_2^2}, \quad (12)$$

where

$$\mu_k = \frac{1}{N} \sum_{i=1}^N |h_i|^k, \quad (13)$$

and where N is the number of spatial sampling points and h_i is the complex amplitude of the i th path.

A scatter plot of the m -factor estimates for the first 200 ns of delay bins for the receiving antenna mounted on the headrest at row 19 is shown in Figure 7(a). Although a few MPCs at the beginning of the PDP (typically when the delay is less than 30 ns) exhibit large m -factors, the vast majority of the 1501 MPCs shown in Figure 7(a) exhibit m -factors of approximately 1 and, as noted previously, their fading distributions are therefore well approximated by Rayleigh statistics. The fading distributions of MPCs observed at the armrest and footrest are also well approximated by Rayleigh statistics.

Other researchers have found that the m -parameter follows a lognormal distribution given by

$$f(m) = \frac{1}{\sigma_m x \sqrt{2\pi}} \exp\left(-\frac{(\ln m - \mu_m)^2}{2\sigma_m^2}\right), \quad (14)$$

where μ_m and σ_m are the mean and variance of the m -factors and are by convention given in decibels [19],[21]. The initial impulses in the PDP for the LOS channel are characterized by a deterministic m -factor, m_0 , which is typically much larger than m at other delays. In [3], it was found that both μ_m and σ_m may depend on the delay of the MPC within the CIR. As shown in Figure 7(a), we did not find any evidence of such dependence. We also observe that m_0 tends to decrease with increasing distance, while μ_m and σ_m are effectively independent of distance. Accordingly, we have characterized μ_m and σ_m simply by taking the average over all distances in each case and we model m_0 by

$$m_0(d) = m_{00} - \beta_{m0} \cdot 10 \log_{10} d + X_{m0}, \quad (15)$$

where m_{00} is the intercept and β_{m0} is the slope, X_{m0} is a zero-mean Gaussian random variable with standard deviation σ_{m0} , and d is the distance between the transmitting and receiving antennas. The small-scale fading parameters that we extracted are summarized in Table IV. The CDF of the estimated m -factors is compared to the CDF of the best-fit lognormal distribution for the case of the receiving antenna mounted on the headrest at row 19 in Figure 7(b). The 12 strongest taps (out of 1501 taps in total) deviate greatly from the lognormal distribution. They correspond to a few strong impulses that arrived near the leading edge of the response and we consider

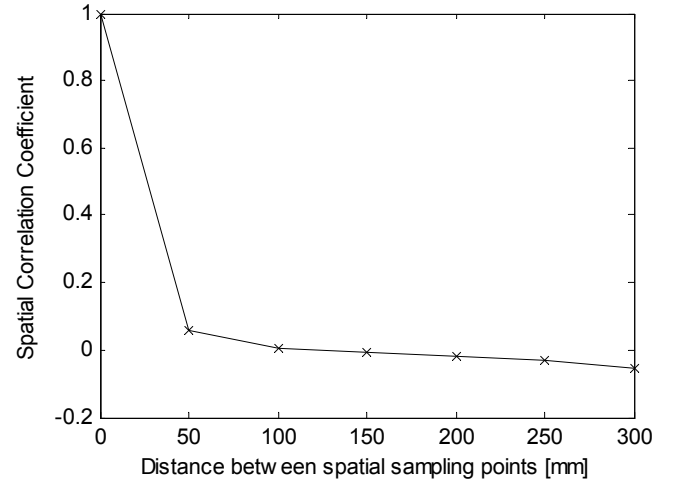


Fig. 8. Spatial correlation averaged over delay as a function of distance between spatial sampling points when the receiving antenna is mounted on the headrest of row 19.

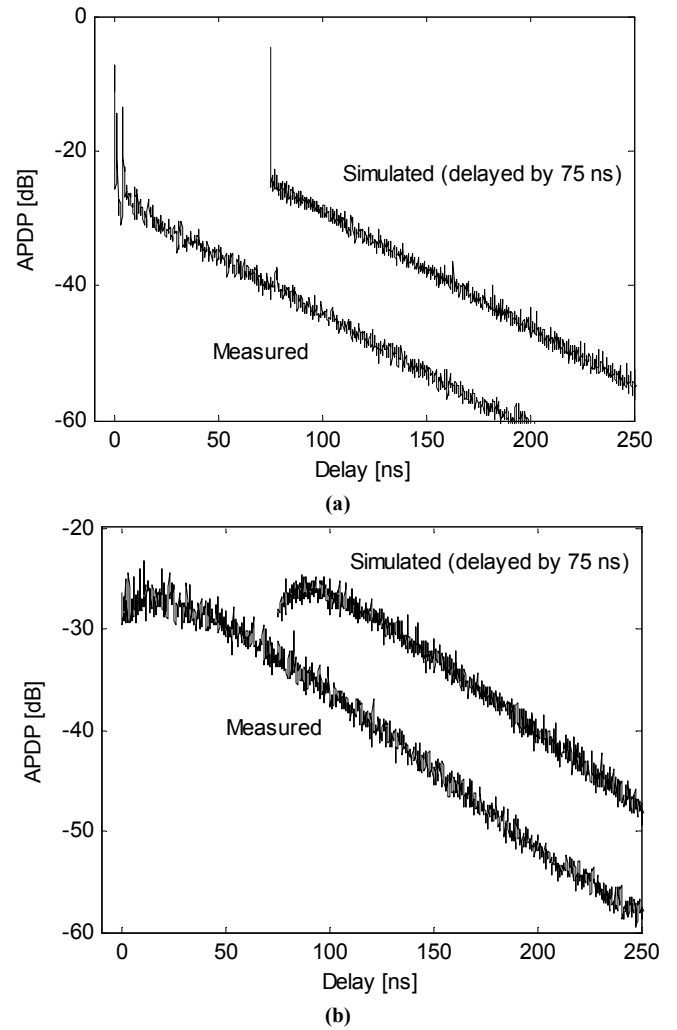


Figure 9 – Comparison of the measured and regenerated APDP for receiving antennas mounted at the (a) headrest and (b) footrest.

them to be outliers.

B. Interdependence of MPCs

The fading correlation between MPCs that are either: (1) in adjacent delay bins with the antenna at the same point on the sampling grid, which we shall refer to as temporal correlation, or (2) in the same delay bin but with the antenna at other points on the sampling grid, which we shall refer to as spatial correlation, is of interest for several reasons. First, if the MPCs in *adjacent* delay bins cannot be modeled as independent random variables, then the complexity of the channel model will increase dramatically. Second, we want to verify that the fading observed at a *given* delay at each point in the spatial sampling grid is reasonably independent from that observed at other points in the grid so that we have confidence that we have a sufficient number of independent samples to estimate the fading statistics. Third, some have recently proposed that WiMedia UWB systems be equipped with antenna arrays so that the direction-of-arrival of incoming signals can be estimated and adaptive array techniques can be used to reduce the susceptibility of the system to interfering signals. UWB-MIMO systems have also been proposed. Knowledge of the spatial correlation properties of the channel is required in order to determine the required antenna element spacing [25]. While the spatial correlation results presented here provide a useful first indication, our grid spacing of 5 cm does not allow unambiguous resolution of angular components at higher UWB frequencies. Thus, practical design of adaptive array antennas to be used at higher UWB frequencies will require that our measurements be supplemented by new data with finer spatial resolution.

The temporal correlation is given by

$$\rho_{temp a_k, a_{k+1}} = \frac{E\{(a_k - \bar{a}_k)(a_{k+1} - \bar{a}_{k+1})\}}{\sqrt{E\{(a_k - \bar{a}_k)^2\}E\{(a_{k+1} - \bar{a}_{k+1})^2\}}}, \quad (16)$$

where $E\{\cdot\}$ denotes expectation, a_k and a_{k+1} are the amplitudes of the k th and $(k+1)$ th MPC respectively, as observed in the CIRs measured at all 49 points in the grid, and \bar{a}_k and \bar{a}_{k+1} are the corresponding mean values across all 49 points [4]. For all receiving antenna positions and locations considered, the mean value of the temporal correlation for the different delay taps is 0.13 with no value exceeding 0.56. Because the correlation between MPCs in adjacent delay bins is low, we can reasonably treat the path amplitudes at each delay as uncorrelated independent random variables.

The spatial correlation between the MPCs at a given delay is given by

$$\rho_{spat}(k, d) = \frac{E\{(p_{n,k} - \bar{p}_k)(p'_{n,k} - \bar{p}'_k)\}}{\sqrt{E\{(p_{n,k} - \bar{p}_k)^2\}E\{(p'_{n,k} - \bar{p}'_k)^2\}}}, \quad (17)$$

where $p_{n,k}$ and $p'_{n,k}$ are the amplitudes of the k th MPC in the

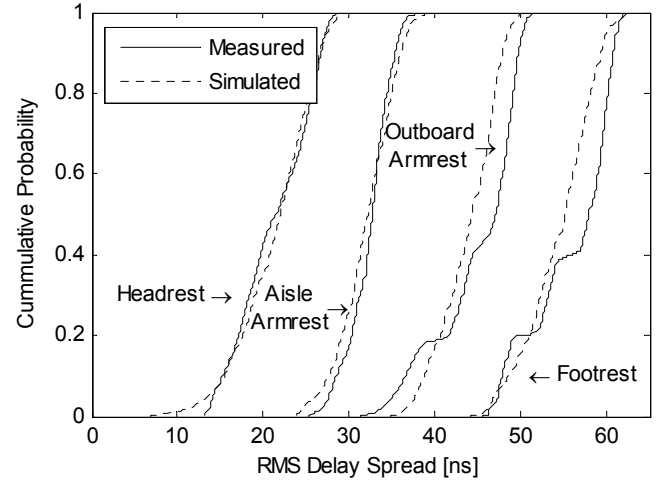


Fig. 10. Distributions of simulated and measured RMS delay spreads for different receiving antenna mounting positions. For clarity, the distributions for the aisle armrest, outboard armrest and footrest cases are offset by 10, 20 and 30 ns, respectively.

PDPs that are observed at the n th pair of points that are separated by a distance d . The parameters \bar{p}_k and \bar{p}'_k are the mean amplitudes seen at all pairs of observation points that satisfy the above criteria [26]. In Figure 8, we show the spatial correlation coefficient as a function of separation distance averaged over all delay bins. When the separation distance is greater than or equal to 50 mm, both the mean and standard deviation of the spatial correlation coefficient are always less than 0.1 and 0.3, respectively. Thus, we can reasonably assume that the path amplitudes observed at any two grid points at the same delay are uncorrelated and that our grid spacing of 50 mm was sufficient for obtaining independent samples for fading statistics estimation. Although this result implies that UWB-MIMO arrays can be realized within aircraft passenger cabins with antenna spacings as small as 50 mm, further measurements will be required to determine if an even smaller spacing is practical.

V. A SIMULATION MODEL FOR UWB CIRs IN AN AIRCRAFT PASSENGER CABIN

With their final report, the IEEE 802.15.4a channel modeling committee released a MATLAB-based simulation code that uses their models to generate CIRs typical of those encountered in residential, office, outdoor and industrial environments. We have modified their channel simulation code so that it can be used to generate UWB CIRs typical of p-to-mp scenarios with the transmitting antenna located at the cabin ceiling and the receiving antenna located at the headrest, armrest and footrest level in the aircraft passenger cabin environment. In our version of the channel simulation code, scenarios AC 1 through AC 4 refer to transmission from the cabin ceiling to the headrest, aisle armrest, outboard armrest and footrest, respectively.

The four main parts of the IEEE 802.15.4a code are concerned with: (1) assignment of the channel model parameters, (2) generation of CIRs using random processes

that simulate: (a) the arrivals of the clusters and rays and (b) the path amplitudes based upon the shape of the PDP and the small-scale fading distribution, (3) prediction of the frequency dependent path loss, and (4) conversion of the result from continuous time to discrete time. The original simulator is based upon statistics that have been averaged over distance.

Here, we use our new models to account for distance explicitly. The headrest and aisle armrest scenarios correspond to LOS channels and the APDPs are modeled by a single exponential decay as described by (4)-(7). The outboard armrest and footrest scenarios correspond to NLOS channels and are modeled using (3) and (8)-(10). Finally, we have modeled the small-scale fading of individual MPCs using (14) and (15). To verify that the modified channel simulator produces reasonable results, we generated CIRs using parameters for a given distance and then compared the results with the measured CIRs observed at the same distance. As shown in Figure 9, the measured and simulated APDPs for both the headrest and outboard armrest scenarios compare well. As shown in Figure 10, the CDFs of the RMS delay spreads associated with measured and simulated CIRs over all ranges between 2 and 13 m also compare well. The authors will supply a copy of the modified version of the channel simulator code upon request.

VI. CONCLUSIONS

Based upon channel response data collected within the passenger cabin of a typical mid-size airliner in p-to-mp configurations, we have proposed a pair of statistical models that describe the UWB channel impulse responses observed over LOS and NLOS channels, respectively. The models describe the shape of the power delay profile, characterize the fading experienced by individual multipath components and give the spatial and delay dependence of the correlation between fading on adjacent MPCs.

We have observed the following trends: (1) For LOS channels, *e.g.*, cabin ceiling to headrest or aisle armrest, the shape of the PDP generally follows IEEE 802.15.4a's dense single-cluster model, but with negligible rise time and, on many occasions, one or more impulses or spikes within 30 ns of the leading edge of the response. (2) For NLOS channels, *e.g.*, cabin ceiling to outboard armrest or footrest, the shape of the PDP follows IEEE 802.15.4a's dense single-cluster model and the rise time is up to 10 ns. (3) The mean and variance of the exponential decay constant (hence the RMS delay spread) tends to increase with path length and as the receiving antenna drops from the headrest to the footrest. (4) Small-scale fading of MPCs tends to follow a Nakagami distribution with a lognormally-distributed m -parameter that is close to 0 dB (which corresponds to Rayleigh fading) with a small variance, as has been found in other rich scattering environments.

In most cases, our results take the form of the parameters of the corresponding models recommended by the IEEE 802.15.4a channel modeling committee and can be used directly in simulations of UWB propagation in an aircraft

interior. Moreover, we have modified the standard channel impulse response simulation code developed by IEEE 802.15.4a so that it can generate CIRs representative of those observed in the aircraft passenger cabin environment. Accordingly, our results will assist: (1) those who are planning UWB deployments and field trials in aircraft and (2) those who need to simulate UWB systems in aircraft using realistic channels.

ACKNOWLEDGMENT

The authors thank Associate Dean Jack Baryluk and Chief Instructor/Hangar Supervisor Grant Johnson of the BCIT Aerospace Technology Campus at Vancouver International Airport for providing us with access to their Boeing 737-200 aircraft and for their outstanding cooperation during the course of this study.

The authors would also like to thank Wadah Muneer, Weiwen Liu, Robert White, Chad Woodworth and Cecelia Yeung for their considerable assistance during the measurement sessions.

REFERENCES

- [1] A. F. Molisch, J. R. Foerster and M. Pendergrass, "Channel models for ultrawideband personal area networks," *IEEE Wireless Commun.*, vol. 10, no. 6, pp. 14-21, Dec. 2003.
- [2] A. F. Molisch, "Ultrawideband propagation channels: Theory, measurement, and modeling", *IEEE Trans. Veh. Technol.*, vol. 54, no.5, pp. 1528-1545, Sep. 2005.
- [3] A. F. Molisch *et al.*, "A comprehensive standardized model for ultrawideband propagation channels," *IEEE Trans. Antennas Propag.*, vol. 54, no. 11, pp. 3151-3165, Nov. 2006.
- [4] C. C. Chong and S. K. Yong, "A generic statistical-based UWB channel model for high-rise apartments," *IEEE Trans. Antennas Propag.*, vol. 53, no. 8, pp. 2389-2399, Aug. 2005.
- [5] A. Jahn *et al.*, "Evolution of aeronautical communications for personal and multimedia services," *IEEE Commun. Mag.*, vol. 41, no. 7, pp. 36-43, Jul. 2003.
- [6] J. J. Ely, W. L. Martin, G. L. Fuller, T. W. Shaver, J. Zimmerman and W. E. Larsen, "UWB EMI to aircraft radios: field evaluation on operational commercial transport airplanes," in *Proc. Digital Avionics Syst. Conf. 2004*, 24-28 Oct. 2004, pp. 9.D.4-1--9.D.4-11.
- [7] J. J. Ely, W. L. Martin, T. W. Shaver, G. L. Fuller, J. Zimmerman and W. E. Larsen, "UWB EMI to aircraft radios: field evaluation on operational commercial transport airplanes," NASA TP-2005-213606 Vol. 1, Jan. 2005.
- [8] N. R. Diaz and M. Holzbock, "Aircraft cabin propagation for multimedia communications," in *Proc. EMPS 2002*, 25-26 Sep. 2002, pp. 281-288.
- [9] N. R. Diaz and J. E. J. Esquitino, "Wideband channel characterization for wireless communications inside a short haul aircraft," in *Proc. IEEE VTC 2004 - Spring*, 17-19 May 2004, pp. 223-228.
- [10] S. Fisahn, M. Camp, N. R. Diaz, R. Keibel and H. Garbe, "General analysis of leaky section cables for multi-band aircraft cabin communications with different measurement techniques," in *Ultra-Wideband Short-Pulse Electromagnetics 7*, 12-16 Jul. 2004, pp. 509-516.
- [11] G. Hankins, L. Vahala and J. H. Beggs, "Propagation prediction inside a B767 in the 2.4 GHz and 5 GHz radio bands," in *2005 IEEE AP-S Int. Symp. Dig.*, 3-8 Jul. 2005, pp. 791-794.
- [12] C. P. Niebla, "Topology and capacity planning for wireless heterogeneous networks in aircraft cabins," in *Proc. IEEE PIMRC 2005*, 11-14 Sep. 2005, pp. 2088-2092.
- [13] G. A. Breit, H. Hachem, J. Forrester, P. Guckian, K. P. Kirchoff and B. J. Donham, "RF propagation characteristics of in-cabin CDMA mobile phone networks," in *Proc. Digital Avionics Syst. Conf. 2005*, 30 Oct.-3 Nov. 2005, pp. 9.C.5-1--9.C.5-12.

- [14] R. Bhagavatula, R. W. Heath and S. Vishwanath, "Optimizing MIMO antenna placement and array configuration for multimedia delivery in aircraft," in *Proc. IEEE VTC 2007 – Spring*, 22-25 Apr. 2007, pp. 425-429.
- [15] J. Chuang, N. Xin, H. Huang, S. Chiu and D. G. Michelson, "UWB radiowave propagation within the passenger cabin of a Boeing 737-200 aircraft," in *Proc. IEEE VTC 2007 – Spring*, 22-25 Apr. 2007, pp. 496-500.
- [16] J. Jemai *et al.*, "UWB channel modeling within an aircraft cabin," in *Proc. IEEE ICUWB 2008*, 10-12 Sep. 2008, pp. 5-8.
- [17] J. Wang, A. S. Mohan and T. A. Aubrey, "Angles-of-arrival of multipath signals in indoor environments," in *Proc. IEEE VTC 1996*, 28 Apr. – 1 May 1996, pp. 155-159.
- [18] D. Porrat and Y. Serfaty, "Sub-band analysis of NLOS indoor channel responses," in *Proc. IEEE PIMRC 2008*, 15-18 Sept. 2008, pp. 1-5.
- [19] C. W. Kim, X. Sun, L. C. Chiam, B. Kannan, F. P. S. Chin and H. K. Garg, "Characterization of ultra-wideband channels for outdoor office environment," in *Proc. IEEE WCNC*, 13-17 Mar. 2005, pp. 950-955.
- [20] D. Cassioli, M. Z. Win and A. F. Molisch, "The ultra-wide bandwidth indoor channel: From statistical model to simulations," *IEEE J. Sel. Areas Commun.*, vol. 20, no. 6, pp. 1247-1257, Aug. 2002.
- [21] J. Karedal, S. Wyne, P. Almers, F. Tufvesson and A. F. Molisch, "A measurement-based statistical model for industrial ultra-wideband channels," *IEEE Trans. Wireless Commun.*, vol. 6, no. 8, pp. 3028-3037, Aug. 2007.
- [22] J. A. Dabin, A. M. Maimovich and H. Grebel, "A statistical ultra-wideband indoor channel model and the effects of antenna directivity on path loss and multipath propagation," *IEEE J. Sel. Areas Commun.*, vol. 24, no. 4, pp. 752-758, Apr. 2006.
- [23] S. S. Ghassemzadeh, L. J. Greenstein, T. Sveinsson, A. Kavcic and V. Tarokh, "UWB delay profile models for residential and commercial indoor environments," *IEEE Trans. Veh. Technol.*, vol. 54, no. 4, pp. 1235-1244, Jul. 2005.
- [24] A. Abdi and M. Kaveh, "Performance comparison of three different estimators for the Nakagami m parameter using Monte Carlo simulation," *IEEE Commun. Lett.*, vol. 4, no. 4, pp. 119-121, Apr. 2000.
- [25] A. K. Marath, A. R. Leyman and H. K. Garg, "DOA estimation of multipath clusters in WiMedia UWB systems," in *Proc. IEEE SAM'08*, 21-23 Jul. 2008, pp. 108-112.
- [26] K. Makaratat and S. Stavrou, "Spatial correlation technique for UWB antenna arrays," *Electron. Lett.*, vol. 42, no. 12, pp. 675-676, 8 Jun. 2006.



David G. Michelson (S'80-M'89-SM'99) received the B.A.Sc., M.A.Sc., and Ph.D. degrees in Electrical Engineering from the University of British Columbia (UBC), Vancouver, BC, Canada.

From 1996 to 2001, he served as a member of a joint team from AT&T Wireless Services, Redmond, WA, and AT&T Labs-Research, Red Bank, NJ, where he was concerned with the development of propagation and channel models for next-generation and fixed wireless systems. The results of this work formed the basis for the propagation and channel models later adopted by the IEEE 802.16 Working Group on Broadband Fixed Wireless Access Standards. From 2001 to 2002, he helped to oversee the deployment of one of the world's largest campus wireless local area networks at UBC while also serving as an Adjunct Professor with the Department of Electrical and Computer Engineering. Since 2003, he has led the Radio Science Laboratory, Department of Electrical and Computer Engineering, UBC, where his current research interests include propagation and channel modeling for fixed wireless, ultra wideband, and satellite communications.

Prof. Michelson is a registered professional engineer. He serves as the Chair of the IEEE Vehicular Technology Society Technical Committee on Propagation and Channel Modeling and as an Associate Editor for Mobile Channels for IEEE Vehicular Technology Magazine. In 2002, he served as a Guest Editor for a pair of Special Issues of the IEEE JOURNAL ON SELECTED AREAS IN COMMUNICATIONS concerning propagation and channel modeling. From 2001 to 2007, he served as an Associate Editor for the IEEE TRANSACTIONS ON VEHICULAR TECHNOLOGY. From 1999 to 2007, he was the Chair of the IEEE Vancouver Section's Joint Communications Chapter. Under his leadership, the chapter received Outstanding Achievement Awards from the IEEE Communications Society in 2002 and 2005 and the Chapter of the Year Award from IEEE Vehicular Technology Society in 2006. He received the E. F. Glass Award from IEEE Canada in 2009 and currently serves as Chair of IEEE Vancouver Section.



Simon Chiu was born in Hong Kong, China in 1984. He received the B.A.Sc. and M.A.Sc. degrees in Electrical Engineering from the University of British Columbia, Vancouver, BC, Canada in 2006 and 2009, respectively.

His main research interests focus on UWB propagation in passenger aircraft cabins and outdoor industrial environments, including the effects of human presence.



James Chuang was born in Tainan, Taiwan in 1982. He received the B.A.Sc. and M.A.Sc. degrees in Electrical Engineering from the University of British Columbia, Vancouver, BC, Canada in 2004 and 2007, respectively.

His main research interests focus on UWB propagation in passenger aircraft cabins and computer-assisted identification of clusters in UWB channel impulse responses.